

# Exploring the high pressure phase diagram of $\text{La}_{1-x}\text{Ca}_x\text{MnO}_3$

A. Sani

*European Synchrotron Radiation Facility, BP 220, F-38043 Grenoble, France*

C. Meneghini\* and S. Mobilio

*Dip. di Fisica Univ. di "Roma Tre" Via della vasca navale 84 I-00146 Roma Italy<sup>†</sup>*

Sugata Ray and D. D. Sarma

*Solid State and Structural Chemistry Unit, Indian Institute of Science, Bangalore 560012, India*

J. A. Alonso

*Instituto de Ciencia de Materiales, CSIC, Cantoblanco, Madrid, E-28049, Spain*

(Dated: November 2, 2018)

The structure of  $\text{La}_{1-x}\text{Ca}_x\text{MnO}_3$  solid solutions ( $x=0, 0.25, 0.50, 0.67, 1$ ) under high pressure (up to 40-45 GPa) has been investigated by synchrotron X-ray powder diffraction (XRD) in order to characterize their volume *vs.* pressure (P-V) equation of state. All the members of the solid solution, except the extreme compounds:  $\text{LaMnO}_3$  and  $\text{CaMnO}_3$ , present low pressure orthorhombic  $Pnma$  phase evolving toward an high pressure tetragonal ( $I4/mcm$ ) symmetry. The details of this transition are related to the Ca doping: on increasing the Ca content, the critical pressure of the transition decreases, but the energetic cost of the transition increases. This study depicts a peculiar evolution of structural distortions as a function of pressure and concentration.

## I. INTRODUCTION

Manganese oxides with perovskite structure form solid solutions of the type:  $(\text{ReMnO}_3)_{1-x}(\text{MeMnO}_3)_x$ , in which trivalent rare earth ions ( $\text{Re} = \text{La, Pr, Y}$ ) are progressively substituted with divalent metal ions ( $\text{Me} = \text{Ca, Ba, Sr}$ ). This substitution produces a mixed-valence state of  $\text{Mn}^{3+}$  and  $\text{Mn}^{4+}$  ions giving rise to a phase diagram rich in interesting transitions and phenomena such as metal to insulator transition (MI), magnetoresistance (MR) and charge ordering (CO) effects. Some of these oxides, in a range of composition, are ferromagnetic metals at low temperatures and become insulator above the Curie temperature ( $T_c$ ). Crossing  $T_c$  is often associated with a large magnetoresistance effect that stimulated the research interest since the early 1950's<sup>1</sup>. In the last decade the discovery of huge magnetoresistance in some of these compounds, named Colossal Magnetoresistance (CMR), renewed intense attention on these materials; besides their potential applications, these compounds are intriguing from a fundamental point of view in the field of strongly correlated systems.

The special features of manganese oxide perovskites originate from a delicate balance among structural, magnetic and electronic degrees of freedom whose main ingredients are: the double exchange (DE) and super-exchange (SE) interactions between Mn ions, plus the coupling between charge carrier and lattice distortions driven by the Jahn-Teller effect on  $\text{Mn}^{3+}$  ions. The concept of DE was introduced<sup>1,2,3</sup> long ago to describe the essential interactions among Mn ions giving rise to the MR effect: the DE, in fact, is dependent on the electron hopping probability  $t$ , between  $\text{Mn}^{3+}$  and  $\text{Mn}^{4+}$  ions. The  $t$  is affected by the relative alignment of  $\text{Mn}^{4+}/\text{Mn}^{3+}$  core

spin ( $t_{2g}$ ) owing to the strong Hund coupling between  $t_{2g}$  and  $e_g$  electron spins. Thus, an external magnetic field which aligns the  $t_{2g}$  spins, promotes the  $e_g$  charge hopping, producing a negative MR effect. The relevance of charge to lattice coupling (e-p), driven by the Jahn-Teller effect on  $\text{Mn}^{3+}$  ions, has been recognized only recently<sup>4,5</sup>: it provides the localization energy to drive the metallic state to an insulator below the room temperature and is essential to explain the huge MR effect. Finally the SE coupling, that is responsible for antiferromagnetic (AFM) interaction between the  $t_{2g}^3$  states at neighboring sites, is a fundamental ingredient stabilizing charge ordered phases in the  $x \geq 0.5$  compounds.

The  $\text{La}_{1-x}\text{Ca}_x\text{MnO}_3$  series of solid solutions is the prototype of mixed-valence perovskites, with similar ionic sizes of Ca and La allowing one to obtain solid solution over the entire concentration range. The phase diagram of  $\text{La}_{1-x}\text{Ca}_x\text{MnO}_3$ , in terms of magnetic, electronic and structural properties as a function of temperature and composition appears complex<sup>6</sup>: around (and above) room temperature (RT) all the compounds are paramagnetic insulators (PM-I). Ca doped compounds, in the  $\sim 0.2 \leq x < 0.5$  composition range, exhibit a paramagnetic-insulator (PM-I) to ferromagnetic-metallic (FM-M) phase transition upon cooling. The transition temperatures ( $T_c$ - $T_{MI}$ ) can be tuned by applying a magnetic field and this gives rise to the so called CMR effect. In the La doped compounds (that is in the  $0.5 \leq x < 0.85$  range) the prevalence of the AFM super-exchange coupling among Mn ions results in low temperature charge ordered (CO) phases that are insulating due to the reduced DE coupling<sup>7</sup>. In a narrow region of composition around  $x = 0.5$  the competition between the FM double exchange and the AFM super-exchange coupling makes the magnetic, electronic and structural phase diagram

highly intricate with the appearance of complex charge ordered superstructures<sup>8</sup>.

It is well-known that the atomic structure of these systems influences the electronic and magnetic structures in diverse ways. From the structural point of view  $\text{LaMnO}_3$  ( $\text{Mn}^{3+}$  ions) is only made of Jahn-Teller (JT) distorted  $\text{MnO}_6$  octahedra while, in the  $\text{CaMnO}_3$  ( $\text{Mn}^{4+}$  ions), the  $\text{MnO}_6$  octahedra are undistorted. The doped compounds show a complex behaviour as a function of temperature and doping: large JT effect is observed in the high temperature PM-I phase, whose amplitude decreases with increasing the Ca content<sup>9,10,11,12</sup>. A sudden drop of  $\text{MnO}_6$  JT distortions accompanies the insulator to metal transition on cooling the sample ( $0.2 \leq x < 0.5$ ) across  $T_c$ - $T_{MI}$ <sup>9,13,14,15</sup>. The low temperature CO phases observed in La doped oxides ( $x \geq 0.5$ ) are characterized by large cooperative JT effect enhancing the  $\text{MnO}_6$  coherent distortions<sup>16</sup>. Not only the long range geometric structure, but also the local structural aspects over the short and medium ranges have profound influence on the physical properties of Mn perovskites, as they determine the relative strengths of various interactions involved. Thus, structural deformation, which modifies the distance between Mn ions, the Mn-O-Mn bond angle and the cell volume, strongly affects the physical properties of the compound such as the electrical conductivity, the magnetic response,  $T_c$ ,  $T_{MI}$  and so on<sup>17,18</sup>.

Relevant information on the physics of these materials can be derived from studies under high pressure<sup>19,20,21,22,23,24</sup> since squeezing the structure is a way to alter the scale of the interactions involved. Studies as a function of hydrostatic pressure, in the relatively low pressure region (up to 2-3 GPa) reported the increase of charge delocalization<sup>19,23</sup> and suggested, in accordance with chemical pressure results, a progressive metallization of the system in the higher pressure region. However, recently, complementary observations from Raman<sup>25</sup> and IR<sup>26</sup> spectroscopy, as well as electrical conductivity and X-ray diffraction (XRD)<sup>27</sup> on  $\text{La}_{0.75}\text{Ca}_{0.25}\text{MnO}_3$  under higher pressures (up to about 12 GPa) have reported the occurrence of a competing mechanism which is activated raising the pressure above 6-7 GPa. This mechanism appears to compete with the charge delocalization preventing the metallization of the system raising the pressure at least till 12 GPa. These recent findings strongly suggest the need for a systematic investigation of the high pressure properties of these compounds.

In this work we describe the structural phase diagram of  $\text{La}_{1-x}\text{Ca}_x\text{MnO}_3$  compounds as a function of pressure up to about 40 GPa and composition ( $0 \leq x \leq 1$ ), thereby providing a complete description of this interesting class of systems. The crystallographic structure of the samples has been studied by synchrotron radiation XRD technique.

## II. EXPERIMENTAL AND DATA ANALYSIS

$\text{La}_{1-x}\text{Ca}_x\text{MnO}_3$  samples were prepared by conventional solid-state reaction method using  $\text{La}_2\text{O}_3$ ,  $\text{CaCO}_3$  and  $\text{Mn}_3\text{O}_4$  precursors mixed in stoichiometric proportions. Soft chemistry procedures have been employed to prepare the stoichiometric  $\text{LaMnO}_3$  and  $\text{CaMnO}_3$  oxides. Stoichiometric amounts of analytical grade  $\text{La}_2\text{O}_3$ ,  $\text{Ca}(\text{NO}_3)_2$  and  $\text{MnCO}_3$  were dissolved in citric acid. The citrate solutions were slowly evaporated, leading to organic resins containing a random distribution of the involved cations at an atomic level. All the organic materials were eliminated in a treatment at 700°C in air, for 12 hours. This treatment gave rise to highly reactive precursor materials, amorphous to X-ray diffraction (XRD).  $\text{LaMnO}_3$  precursor was then treated at 1100°C in a  $\text{N}_2$  flow for 12 hours: inert-atmosphere annealing was required to avoid the formation of oxidized  $\text{LaMnO}_{3+\delta}$  phases (rhombohedral in symmetry), thus minimizing the unwanted presence of  $\text{Mn}^{4+}$ .  $\text{CaMnO}_3$  precursor was annealed in air at 1100°C for 12 h. All the compounds appear single phase at standard X-ray diffraction analysis.

High pressure X-ray Diffraction experiments were performed at the high pressure beam line (ID9) of the European Synchrotron Radiation Facility (ESRF) in Grenoble (France). Powder diffraction patterns were collected using an angle dispersed set-up based on a MAR345 imaging plate detector. The monochromatic beam ( $\lambda = .41436$  Å) was focussed to  $30 \times 30 \mu\text{m}^2$  spot using a Pt-coated mirror (vertical focus) and an asymmetrically cut bent Si (111) Laue monochromator (horizontal focus)<sup>28</sup>. Hydrostatic compression was achieved in a "Le Toullec" type diamond anvil cell (DAC). The diameter of the diamond culet was  $300 \mu\text{m}$ , smaller than in our previous experiment<sup>(27)</sup> but it is mandatory in order to reach higher pressures. A stainless steel gasket with a  $125 \mu\text{m}$  hole diameter was used. Finely ground sample powder was placed in the gasket hole using nitrogen as pressure transmitting media. The diamonds, mounted with a thrust axis parallel to the incident beam, allowed collecting a diffraction cone of about  $25^\circ$  in  $2\theta$ . The collection time was fixed to 5 s for each sample. The DAC oscillates in between  $\pm 3^\circ$ . during acquisition in order to improve the statistics over the sample orientations. The pressure on the sample was determined before and after each imaging, by monitoring the fluorescence line shift of a small ruby pellet enclosed in the DAC with the sample.<sup>29</sup> XRD patterns were collected at room temperature in the pressure range 0-40 GPa with steps of about 1 GPa. 2D-XRD patterns were collected on a MAR345 Imaging Plate (IP) with a pixel dimension of  $100 \times 100 \mu\text{m}^2$  placed about 300 mm from the sample. With this set-up, the angular resolution calibrated on Si-NBS, was of about  $0.04^\circ$  FWHM in  $2\theta$ . The images were treated using the FIT2D package<sup>30</sup> in order to have standard intensity vs.  $2\theta$  patterns, corrected for geometrical effects. Structural refinement of integrated profile patterns was achieved through the Ri-

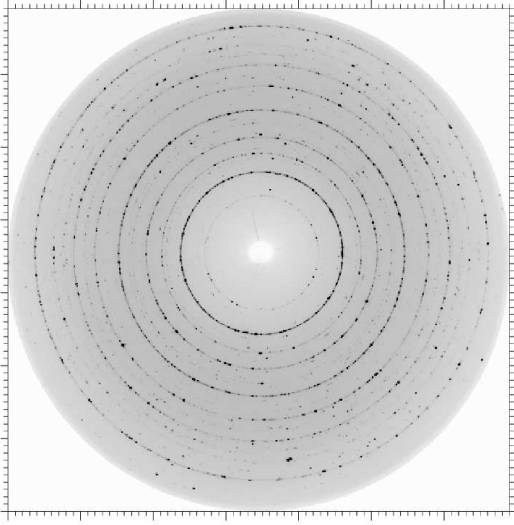


FIG. 1: Typical 2D XRD pattern as collected using the MAR345 detector.

etveld method as implemented in the GSAS package.<sup>31</sup> Pseudo-Voigt profile function proved to be appropriate to fit the experimental pattern without asymmetry correction. The background was modelled using a 12 term expansion of the Chebychev polynomial function.

In figure 1, a raw 2D XRD pattern image as collected from a perovskite sample is presented. The very reduced sample volume probed by the XRD beam (being  $\approx 10^{-9} \text{cm}^3$ ) produces large orientational effect as shown by the inhomogeneous intensity distribution along the Debye rings. It is clear that the angular dispersed set-up and the 2D detector are mandatory for such a kind of experiments since it represents the only way to recover the preferred orientation effect and obtain a reliable pattern intensity. In addition the MAR345 detector allows collecting data of high quality thanks to the high count statistics, to its linearity and to the rapid acquisition time avoiding for pressure gradients during collection. It is important to note that this detector allows reading in situ the 2D patterns, this avoids incertitude in the experimental geometry calibration (beam center, sample to detector distances, detector tilts) that, on the contrary, may cause larger problems using ex-situ IP read-out devices.

Before we proceed to the data presentation and to the discussion of the results it is worth while to notice that though the absolute accuracy of XRD pattern analysis can be affected by the calibration procedure (beam wavelength, sample to detector distance and so on), the relative modifications of XRD patterns induced by the pressure is reliable being largely independent of such factors. Thus, structural evolution under pressure and, more in general, relative changes in structural features, can be followed with very high accuracy with this set up, arising from the exceptional statistics and the integration

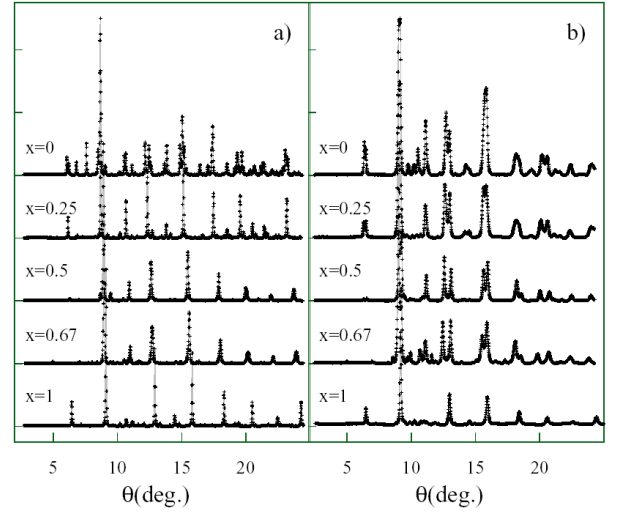


FIG. 2: XRD patterns for the five samples investigated at low pressure ( $P \approx 3 \text{GPa}$ , panel a) depict the same  $Pnma$  space group symmetry. The high pressure phases ( $P \approx 30 \text{GPa}$ , panel b) are function of the sample composition:  $x=0$  sample present  $Imma$  orthorhombic phase,  $x=0.25, 0.5$  and  $0.67$  have tetragonal  $I4/mcm$  high pressure phase,  $x=1$  has orthorhombic  $Pnma$  phase in the whole pressure range investigated.

over the whole Debye rings allowing also weak pattern modifications to be recognized.

The equation of state has been quantitatively analyzed by fitting the  $V$  vs.  $P$  curves with the Birch-Murnaghan (B-M) equation of state<sup>32</sup>. The B-M equation is based on the assumption that the strain energy can be expressed as a Taylor series in the finite strain  $f$ . There are several alternative definitions for  $f$  corresponding to different equation of state, each one leading to a different relationship between  $P$  and  $V$ . The B-M equation is based on the so called Eulerian definition of  $f$  that is:

$$f_E = \frac{1}{2} \left[ (V_0/V)^{2/3} - 1 \right] \quad (1)$$

and the expansion to the fourth order in the strain yields:

$$P = 3B_0 f_E (1 + 2f_E)^{5/2} \left[ 1 + \frac{3}{2} (B' - 4) f_E + \frac{3}{2} \left( B_0 B'' + (B' - 4)(B' - 3) + \frac{35}{9} \right) f_E^2 \right] \quad (2)$$

The bulk modulus at the zero pressure ( $B_0 = -V \partial P / \partial V$ ) and its pressure derivatives ( $B' = \partial B / \partial P$  and  $B'' = \partial^2 B / \partial P^2$ ) characterize the stiffness of the solid. If the equation is truncated at the second order in the energy, then the coefficient of  $f_E$  must be identical to zero, thus  $B' = 4$ . The truncation to the third order, that implies the coefficient of  $f_E^2$  equals zero, gives a three parameters equation:  $V_0$ ,  $B_0$  and  $B'$ , and implies  $B''_0 = -1/B_0[(3 - B')(4 - B') + 35/9]$ . Within this formalism the normalized pressure is defined as:

TABLE I: Refined structural parameters from synchrotron radiation X-ray diffraction for  $\text{LaMnO}_3$  at selected pressures in the  $Pnma$  and  $Imma$  space groups. Numbers in parentheses are statistical errors at the last significant digit. The atomic positions in the  $Pnma$  are: Mn (0.,0.,0.5); La and O(1) ( $x$ , 0.25,  $z$ ); O(2) ( $x$ ,  $y$ ,  $z$ ). In the  $Imma$  space group the atomic positions are: Mn (0., 0., 0.5); La and O(1) (0., 0.25,  $z$ ) and O(2) (0.25,  $y$ , 0.75).

	2.1 GPa ( <i>Pnma</i> )	16.3 GPa ( <i>Imma</i> )	28.2 GPa ( <i>Imma</i> )
$a$ (Å)	5.6349(4)	5.2703(8)	5.320(2)
$b$ (Å)	7.6912(5)	7.522(1)	7.391(2)
$c$ (Å)	5.5233(4)	5.47323(5)	5.362(2)
$V$ (Å <sup>3</sup> )	329.28(2)	221.10	218.83
La	$x$ 0.0430(5)		
	$z$ 0.9999(1)	-0.001(2)	0.017(1)
O(1)	$x$ 0.497(6)		
	$z$ 0.088(6)	0.083(3)	-0.071(8)
O(2)	$x$ 0.293(5)		
	$y$ 0.034(3)	0.054(2)	-0.035(4)
	$z$ 0.714(7)		
$R_{WP}$ %	2.53	2.30	2.90
$\chi^2$	0.7	0.6	0.6

$F_E = P[3f_E(1 + 2f_E)^{5/2}]^{-1}$  so that the plot  $F_E$  vs.  $f_E$  gives an intuitive way to determine the order of the B-M equation: a constant  $F_E(f_E)$  implies a second order B-M equation of state, a linear trend requires a third order B-M equation and quadratic trend justifies the fitting with a fourth order equation of state.

### III. RESULTS

The figure 2 reports examples of low and high pressure XRD patterns for the investigated samples as a function of composition. Despite the Ca doping,  $0 \leq x \leq 1$ , all the members of the family, at low pressure, represent an orthorhombic structure described by the  $Pnma$  space group. Such a structure is derived from the ideal cubic perovskite structure in which the  $\text{MnO}_6$  octahedra, are located on the cube corners, while the La/Ca ions occupy the cube centers. However, since the La/Ca ions are too small to fill the free space inside the cube (size mismatch), the space filling is achieved mainly by tilting the  $\text{MnO}_6$  octahedra with respect to the crystallographic planes, thus deforming the cube and doubling the unit cell along the  $b$  axis (figure 3a). Within the  $Pnma$  space group description, the lattice parameters ( $a$ ,  $b$ ,  $c$ ) are related to the edge of the ideal perovskite cubic cell  $a_p$ , by  $a = c \sim \sqrt{2}a_p$  and  $b = 2a_p$ . The two inequivalent oxygen sites in the  $Pnma$  structure also allow taking into account the JT distortion of  $\text{MnO}_6$  octahedra observed for  $x < 1$ . High pressure structures are found to depend

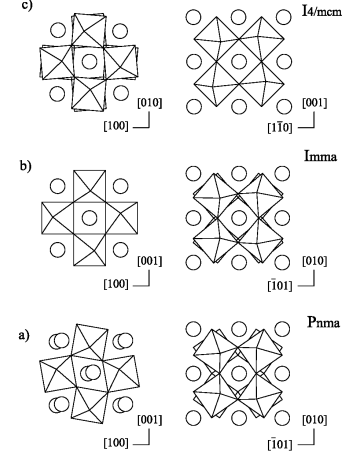


FIG. 3: The main structural features found in the high pressure phase diagram of  $\text{La}_{1-x}\text{Ca}_x\text{MnO}_3$  samples: the orthorhombic  $Pnma$  structure (a) is characterized by three independent Mn-O distances and three tilt modes. The  $Imma$  structure (b) has two independent Mn-O distances and two two tilt modes. The tetragonal  $I4/mcm$  structure (c) has two independent Mn-O distances and one tilt mode.

on the Ca doping: the structure of  $\text{LaMnO}_3$  remains orthorhombic, but the space group changes from  $Pnma$  to  $Imma$  characterized by alternate rotation of the octahedra around the  $[101]$  direction (figure 3b). The high pressure phase in doped compounds ( $0 < x < 1$ ) is tetragonal ( $I4/mcm$ ), characterized by alternate rotation of the octahedra around the  $[001]$  axis (figure 3c). The structure of  $\text{CaMnO}_3$  remains orthorhombic in the  $Pnma$  space group in the whole pressure range investigated.

The structural evolution of the samples as a function of pressure and composition is detailed in the following sections.

#### A. $\text{LaMnO}_3$

Typical diffraction patterns of  $\text{LaMnO}_3$  in the pressure range 1-32 GPa are shown in figure 4 and an example of the profile fitting ( $P=11.7$  GPa) is reported in figure 5. The good data quality allows a satisfactory refinement up to  $P = 32$  GPa yielding reliable lattice parameters and atomic positions.

The figure 6(0.0-a) reports the evolution of  $\text{LaMnO}_3$  lattice edges as a function of pressure. The  $b$ -axis values reported in the figure are normalized by a factor  $1/\sqrt{2}$ , corresponding to a pseudo-cubic representation of the lattice. The compressibility is different along the three axes and evolves differently as a function of the applied pressure as shown by the data reported in figure 6(0.0-a): the  $\text{LaMnO}_3$   $a$ -axis represents the soft compressibility direction up to about 16 GPa, thus the  $a$ -axis compressibility decreases. The  $b$ -axis compressibility changes (slightly

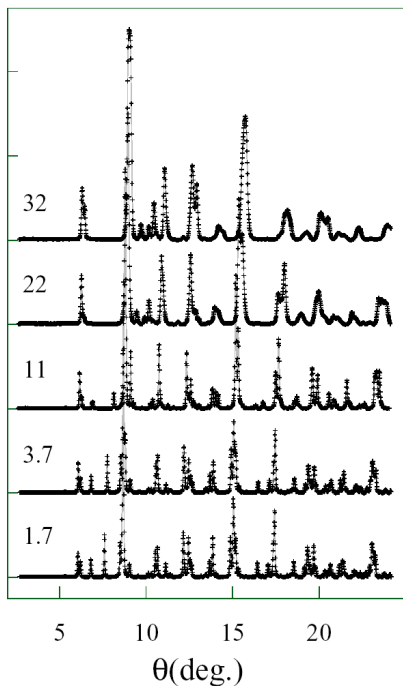


FIG. 4: Selected XRD patterns of  $\text{LaMnO}_3$  as a function of applied pressure collected at RT. Pressure are reported in GPa.

decreases) above  $\approx 20$  GPa. Along the  $c$ -axis, the compressibility decreases smoothly till about 14 GPa and then it abruptly increases above  $\approx 14$  GPa. This trend is in qualitative agreement with that reported recently<sup>33</sup>. The structure of  $\text{LaMnO}_3$  remains orthorhombic up to 35 GPa.

However the changes of compressibility along the three axes in the region 10-20 GPa, are indicative of a phase transition and the progressive decrease of intensity of the (1 1 1) reflection (see figure 4) is suggestive of a  $I$  space group, since the reflections with  $h+k+l$  odd are forbidden by this symmetry. This qualitative hypothesis is further confirmed by the impossibility to achieve satisfactory structural refinement convergence within the  $Pnma$  space group above  $\approx 15$  GPa. The refinements of XRD profiles demonstrate a change of space group from  $Pnma$  to  $Imma$  above  $\approx 15$  GPa, as evidenced by the volume compressibility change visible in figure 6(0.0-b). The  $Imma$  space group is derived from the ideal cubic perovskite structure by a single rotation of the octahedra around the  $[1\ 0\ 1]$  cubic direction (figure 3). This phase has been already observed in manganese oxide perovskites containing cations with a large ionic radius, such as  $\text{La}_{0.70}\text{Ba}_{0.30}\text{MnO}_3$ <sup>34</sup>, as a result of chemical substitution effect. However,  $Pnma$ - $Imma$  transition in the present case of physical pressure does not involve any intermediate trigonal phase that is observed in studies performed as a function of the chemical pressure<sup>34</sup>. The smoothness in the evolution of the cell parameters and

cell volume as a function of applied pressure (figure 6(0.0-a,b)) demonstrate the continuous (second order) nature of this phase transition. The  $V$  vs.  $P$  curve is well described by a third order Birch-Murnaghan equation of state<sup>35</sup>, yielding the values reported in table III for the bulk moduli,  $B_0$  and  $B'$ . These values are in agreement with those reported in literature<sup>33</sup>. The values of  $B'$  (that is 9.5 in the  $Pnma$  phase and 12 in the  $Imma$  phase) are large in comparison to those typical of crystals with nearly isotropic compression that ranges in between 4-6. These large values found here must be related to the anisotropic compressibility along the three axes, as already suggested in ref.<sup>33</sup>. The bulk modulus and its derivative increase through the  $Pnma$  to  $Imma$  transition pointing out the increasing stiffness of the structure. The  $Pnma$  to  $Imma$  transition increases the stiffness of the structure with the doubling of the bulk modulus, from about 100 GPa to 200 GPa.

We can clearly notice from fig. 6a that  $a$  and  $c$  axes lengths approach each other raising the pressure toward the maximum value (32 GPa). This trend, in analogy with the results obtained on the other samples (see below), may suggest an impending orthorhombic to tetragonal phase transition which might be reached at somewhat higher pressure.

The good quality of the patterns allows reliable refinement of the atomic positions from which the Mn-O bond distances are calculated, as reported in figure 6(0.0-c). In the  $Pnma$  phase, the three Mn-O distances remain distinguishable, above the statistical uncertainty, till about 14 GPa. This finding, in agreement with recent neutron diffraction results<sup>36</sup>, demonstrates the stability of JT effect even in the high pressure region. The  $Pnma$  to  $Imma$  transition provokes the collapse of the three Mn-O distances into one single value, representing removal of the coherent JT distortion.

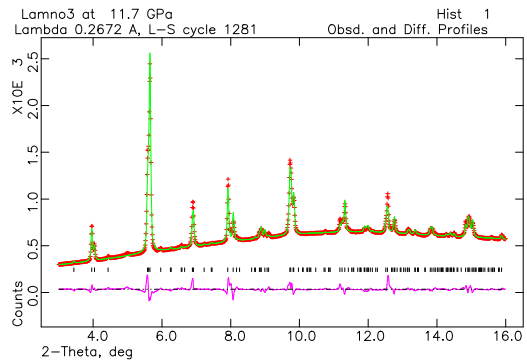


FIG. 5: Example of XRD Rietveld profile refinement on  $\text{LaMnO}_3$  pattern collected at 11.7 GPa. Experimental data (crosses) best fit profile (line) and residual (shifted for clarity) are shown. Markers represent the expected positions for the diffraction lines.

The orthorhombic strains in the  $ac$  plane,  $\text{Os}_{\parallel} = 2(a - c)/(a + c)$ , and along the  $b$  axis with respect to the  $ac$

plane,  $Os_{\perp} = 2(b/\sqrt{2} - (a+c)/2)/(b/\sqrt{2} + (a+c)/2)$ , are reported in figure 6(0.0-d). They represent the deviation of the structure from an ideal cubic cell.  $Os_{\parallel}$  is quite large ( $\sim 2\%$ ) at low pressures decreases to zero ( $a = b$ ) around 10 GPa. Thus it increases in absolute value reaching the  $-2\%$  in between 15 and 25 GPa. The decreasing trend (in absolute value) of  $Os_{\parallel}$  raising the pressure above 25 GPa is one other finding suggesting an incoming tetragonal transition to be reached at higher pressure (see the panel 0.25-d in figure 6). The effect of pressure on the  $Os_{\perp}$  is weaker: in the *Pnma* phase it decreases (in absolute value) from  $-2.8\%$  to about  $-2\%$ , and remains quite unchanged in the high pressure *Imma* phase.

TABLE II: Refined structural parameters from refinement of  $La_{0.75}Ca_{0.25}MnO_3$  XRD patterns at selected pressures in the *Pnma*, *Imma* and *I4/mcm* space groups. Numbers in parentheses are statistical errors at the last significant digit. Example of structural refinement within the *Imma* space group ( $P \sim 20$  GPa) is reported in the third column. The atomic positions in the *Pnma* are: Mn (0., 0., 0.5); La and O(1): ( $x$ , 0.25,  $z$ ); O(2) ( $x, y, z$ ). In the *Imma* space group are: Mn (0., 0., 0.5); La and O(1) (0., 0.25,  $z$ ) and O(2) (0.25,  $y$ , 0.75). In the *I4/mcm* space group the atomic positions are: Mn (0., 0., 0.); La/Ca and O(1) (0., 0., 0.25) and O(2) ( $x$ ,  $x+0.5$ , 0.).

	6.1 GPa	20.2 GPa	27.1 GPa	38.2 GPa
	( <i>Pnma</i> )	( <i>Imma</i> )	( <i>I4/mcm</i> )	( <i>I4/mcm</i> )
$a$ (Å)	5.4133(3)	5.3231(3)	5.2846(6)	5.2050(2)
$b$ (Å)	7.6500(5)	7.4867(1)	7.587(2)	7.561(2)
$c$ (Å)	5.4478(3)	5.3813(1)		
$V$ (Å <sup>3</sup> )	225.61(1)	214.45	211.9	204.84
La/Ca $x$	0.07(1)			
$z$	-0.001(1)	-0.058(6)		
O(1) $x$	0.49(2)			
$z$	0.113(6)	0.059(6)		
O(2) $x$	0.28(1)		0.31(1)	0.32(1)
$y$	0.033(4)	-0.016(4)		
$z$	0.718(8)			
$R_{WP}$ %	3.80	3.07	2.93	2.63
$\chi^2$	0.7	0.4	1.2	0.6

### B. $La_{0.75}Ca_{0.25}MnO_3$

The high pressure structural behavior of  $La_{0.75}Ca_{0.25}MnO_3$  was investigated by some of us in a recent work<sup>27</sup> extending the pressure range up to about 12 GPa. In this experiment we have been able to extend the pressure range up to about 40 GPa by using a smaller diamond culet in the DAC cell. Unfortunately, the quality of the data collected in this sample is slightly poorer than in the previous experiment. This is partially due to the smaller sample volume that reduces the

TABLE III: Bulk moduli at the zero pressure ( $B_0$ ) and their pressure derivatives ( $B'$  and  $B''$ ) derived by fitting the  $V(P)$  data with the B-M equation of state.

$La_{1-x}Ca_xMnO_3$	$B_0$	$B'$	$B''$
phase (GPa)	$B'$	$B''$	(GPa <sup>-1</sup> )
x=0 <i>Pnma</i>	104(2)	9.5(2)	
<i>Imma</i>	200(5)	12.0(6)	
x=0.25 <i>Pnma</i>	136(4)	10.2(3)	
<i>Pnma</i> *	176(6)	3.3(1)	0.9(3)
<i>I4/mcm</i>	310(30)	7(3)	
x=0.5 <i>Pnma</i>	172(5)	5.7(6)	
<i>I4/mcm</i>	253(5)	6.4(8)	
x=0.67 <i>Pnma</i>	210(7)	2(1)	
<i>I4/mcm</i>	186(7)	4(1)	
x=1 <i>Pnma</i> *	195(3)	2.9(2)	0.2(1)

statistics in XRD patterns. For this reason we have a slightly larger uncertainty refining the the lattice parameters and, in particular, refining the Mn and O atomic positions. Notice, however, that the new values are in agreement with those previously reported in the overlapping range (figure 6(0.25)).

The lattice parameters reported in figure 6(0.25-a) depict a decreasing trend as a function of the applied pressure till about 20 GPa. The easy compressibility axis above 10 GPa is the  $b$ -axis. The evolution of the  $b$ -axis as a function of the applied pressure is quite smooth till about 27 GPa. On the contrary, we notice a smooth change of slope in the  $a$  and  $c$ -axes *vs.*  $P$  curves above  $\sim 10$  GPa. Changes in  $a$ - and  $c$ -axes compressibility become more accentuated on raising the pressure above  $\sim 20$  GPa, causing the convergence of  $a$  and  $c$  lattice parameters in the region preceding to the orthorhombic (*Pnma*) to tetragonal (*I4/mcm*) phase transition occurring around 27 GPa. We must notice that the intensity of the (1 1 1) reflection in the XRD patterns becomes progressively weaker on raising the pressure as we already observed in  $LaMnO_3$ . This trend and the change of compressibility along the  $a$ - and  $c$ -axes are compatible with a sluggish *Pnma* to *Imma* phase transition starting around 17-20 GPa. This hypothesis is in agreement with the reported *Pnma* to *I4/mcm* through *Imma* phase transition as a function of average cation size<sup>37</sup>. We must notice, in addition, that we found a progressive increase of the  $\chi^2$  factor refining our XRD patterns above 10-13 GPa. This suggests that the progressive appearance of other crystallographic phases, together with the *Pnma* one, may even be starting at lower pressures. The hypothesis of parasitic phases above  $\sim 10$  GPa is also in agreement with the quadratic trend observed in the plot of the normalized pressure,  $F_E$ , as a function of the Eulerian strain  $f_E$  (see below).

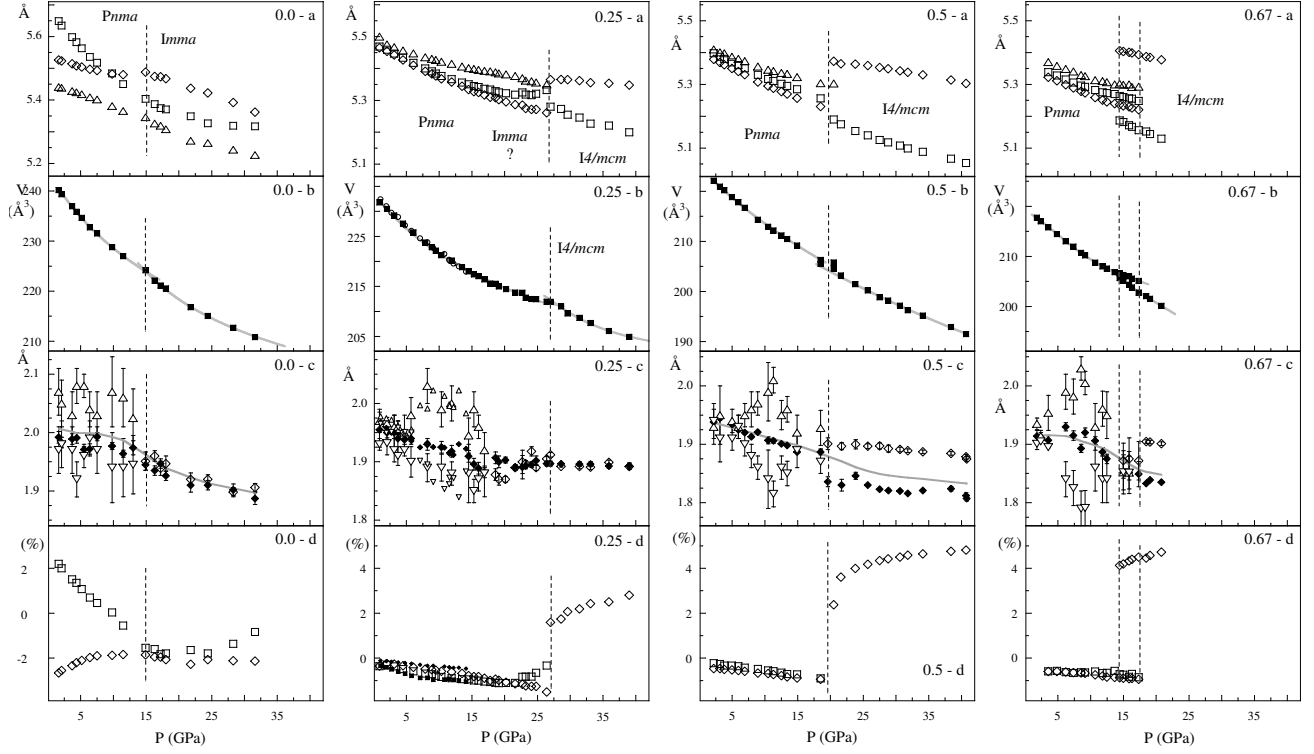


FIG. 6: The principal structural parameters for  $x=0$  (0.0 plots),  $x=0.25$  (0.25 plots),  $x=0.5$  (0.5 plots) and  $x=0.67$  (0.67 plots) samples as a function of the applied pressure. Panels *a* show the lattice parameters ( $a$ =squares,  $b/\sqrt{2}$ =diamonds and  $c$ =triangles). The volume *vs.* pressure data are reported in panels *b* (squares black), the continuous gray lines refer to the fit of the Birch-Murnaghan equation of state. Mn-O distances are shown in panels *c*: three different Mn-O distances are found in the  $Pnma$  phase and only two in the tetragonal phase. The grey line is a smooth fit through the average Mn-O distance points. Panels *d* report the orthorhombic (tetragonal) strain parallel ( $O_{s\parallel}$ ) to the  $ac$  plane (squares) and along  $b$  with respect to the  $ab$  plane ( $O_{s\perp}$ ) (diamonds). For sake of comparison the previous results for  $x=0.25$  sample are also reported in panels 0.25-b (open circles), 0.25-c (small symbols without error bars) and 0.25-d (small diamonds).

The V(P) curve reported in figure 6(0.25-b) depicts an evident change of slope around 27 GPa, in correspondence of the orthorhombic to tetragonal phase transition. The fitting with a third order B-M equation of state<sup>35</sup> in the P less than as well as above 27 GPa allows extracting the values of the bulk moduli in the *Pnma* and *I4/mcm* phases, respectively. We found  $B_0=136$  GPa and  $B' \sim 10$  in the orthorhombic phase, and  $B_0 \approx 300$  GPa and  $B' \sim 7$  in the high pressure tetragonal phase (table III). The values of  $B_0$  and  $B'$  are respectively smaller and larger in the *Pnma* phase than those previously reported<sup>27</sup>, namely  $B_0=178$  GPa and  $B' \sim 4$ . The  $B'$  value is anomalously high, similar to that previously observed in the  $\text{LaMnO}_3$  sample, even if, in this sample the compressibility anisotropy along the three axes is less evident. The figure 8 shows the plot of the normalized pressure,  $F_E$ , as a function of the Eulerian strain  $f_E$  for  $\text{La}_{0.75}\text{Ca}_{0.25}\text{MnO}_3$  sample. In this plot, a non linear trend in the  $F_E(f_E)$  curve is evident, suggesting the fitting with a fourth order B-M equation. In this case the best fit gives the following values for the bulk modulus and its derivatives:  $B_0 = 176$  GPa,  $B' = 3.3$  and  $B'' = 0.9$  GPa<sup>-1</sup>. Notice that in this case the values found for  $B_0$  and  $B'$  are in agreement with our previous findings obtained over a restricted pressure range, and the  $B'$  is consistent with the more isotropic compressibility of the structure. The quadratic trend found in the  $F_E$  vs.  $f_E$  curve could suggest the growing of parasitic phases already around 10 GPa.

Around 25 GPa the orthorhombic structure becomes unstable and the system evolves towards a tetragonal structure (*I4/mcm*). This phase transition is characterized, below the critical pressure, by a sort of plateau of the V(P) curve. The smoothness of the phase transition is characterized by a progressive decrease of  $c$ , which “fuses” with  $a$ . One may wonder why  $b$  increases with pressure, since the compression has commonly a squeezing effect on the lattice parameters. This anomalous effect must stem from a change in the tilt of the octahedra in the new phase. In fact the effect of pressure on the structure is twofold: on one hand, the pressure acts on the size of the Mn octahedra taking it closer to a more symmetric structure characterized by one Mn-O distance. On the other hand, the pressure induced phase transition modifies the tilting of the octahedra (figure 3). The *Pnma* phase is characterized by a three-tilt system of the  $\text{MnO}_6$  octahedra<sup>38</sup> while in the tetragonal structure the octahedra are aligned along the  $b$  axis (Mn-O-Mn bond angle along  $b$  is 180°) thus the cell must expand in this direction in order to accommodate the two Mn-O bonds along  $b$ .

Even if the quality of the data makes the refinement of atomic positions more uncertain with respect to the previous results, we notice that the evolution of Mn-O bond lengths matches well our previous results: at low pressures ( $P < 5-6$  GPa) the Mn-O bond lengths appear indistinguishable within the statistical uncertainty. Above 5-6 GPa three Mn-O distances are recognizable, pointing

out a larger coherent JT effect. The Mn-O bond lengths collapse raising the pressure above  $\sim 15$  GPa, as the structure evolves from the orthorhombic to the tetragonal phase. The Mn-O bonds remain indistinguishable in the high pressure orthorhombic region and in the tetragonal phase demonstrating the absence of any coherent JT effect.

The orthorhombic strains (figure 6(0.25-d)) are sensibly lower than in the  $\text{LaMnO}_3$  sample. Consistently with our previous results both  $\text{Os}_\perp$  and  $\text{Os}_\parallel$  decreases (increases in absolute value) as a function of the applied pressure. Raising the pressure above 20 GPa causes  $\text{Os}_\parallel$  to approach zero before the transition to the tetragonal phase. In the *I4/mcm* phase  $a = b$  causes  $\text{Os}_\parallel = 0$ . The  $\text{Os}_\perp$  increases (in absolute value) as a function of pressure in the whole range investigated. The change of symmetry causes the change of sign  $\text{Os}_\perp$  but its modulus evolves smoothly across the phase transition.

TABLE IV: Refined structural parameters from refinement of  $\text{La}_{0.5}\text{Ca}_{0.5}\text{MnO}_3$  XRD patterns at selected pressures in the *Pnma* and *I4/mcm* space groups. Numbers in parentheses are statistical errors at the last significant digit. The atomic positions in the *Pnma* are: Mn (0., 0., 0.5); La and O(1): ( $x$ , 0.25,  $z$ ); O(2) ( $x,y,z$ ). In the *I4/mcm* space group the atomic positions are: Mn (0., 0., 0.); La/Ca and O(1) (0., 0., 0.25) and O(2) ( $x$ ,  $x+0.5$ , 0.).

	5.9 GPa ( <i>Pnma</i> )	20.1 GPa ( <i>I4/mcm</i> )	40.7 GPa ( <i>I4/mcm</i> )
$a$ (Å)	5.3605(2)	5.1536(3)	5.0533(5)
$b$ (Å)	7.5532(2)	7.5853(7)	7.499(1)
$c$ (Å)	5.3803(2)		
$V$ (Å <sup>3</sup> )	217.85(1)	201.47	191.49
La/Ca	$x$ 0.0157(4)		
	$z$ -0.0035(3)		
O(1)	$x$ -0.0061(3)		
	$z$ 0.4306(2)		
O(2)	$x$ 0.718(4)	0.756(1)	0.790(3)
	$y$ -0.032(1)		
	$z$ 0.280(3)		
$R_{WP}$ %	1.60	3.59	4.37
$\chi^2$	0.2	1.4	1.85

### C. $\text{La}_{0.5}\text{Ca}_{0.5}\text{MnO}_3$

The structural refinement of  $\text{La}_{0.5}\text{Ca}_{0.5}\text{MnO}_3$  diffraction pattern as a function of applied pressure shows that the samples are metrically orthorhombic in the low pressure region and the structure belongs within the *Pnma* space group up to 18 GPa. Above this pressure new peaks appear that cannot be indexed within the *Pnma* space group. Similar to the case of  $x=0.25$  sample, the high pressure phase turns out to be tetragonal with

$I4/mcm$  space group. The transition is well evident from the evolution of lattice parameters (Fig. 6(0.5-a)). The two phases,  $Pnma$  and  $I4/mcm$ , coexist in a reduced region around the transition. Before the transition, we do not observe the sluggish evolution seen for the  $x=0.25$  sample and also the quality of the structural refinement ( $\chi^2$ ) remains good in the whole range allowing to exclude the presence of other phase transitions between the orthorhombic-to-tetragonal one.

Fitting the  $V(P)$  curve with the B-M equation<sup>35</sup> in the  $Pnma$  ( $I4/mcm$ ) phase results in a bulk modulus  $B_0=172$  GPa ( $B_0=253$  GPa) and its pressure derivative  $B'=5.7$  ( $B'=6.4$ ) (table III). As for  $x=0.25$  sample, the bulk modulus for  $x=0.5$  sample is larger in the  $I4/mcm$  phase pointing out the reinforcement of stiffness through the orthorhombic-to-tetragonal transition.

$\text{La}_{0.5}\text{Ca}_{0.5}\text{MnO}_3$  has three independent Mn-O distances in the orthorhombic phase reported in figure 6(0.5-c). At low pressures, the  $\text{MnO}_6$  octahedron has six almost equal distances. As the pressure increases above  $\approx 6$  GPa we observe the progressive splitting of the three Mn-O distances till about 10 GPa where the JT effect reaches the maximum distortion value of about 0.07 Å. At still higher pressures, the Mn-O distances approach each other reducing the JT distortion (figure 6(0.5-c)) just before the orthorhombic to tetragonal transition. Nevertheless, in contrast to the  $x=0.25$  sample, structural refinement gives two distinct Mn-O distances in the  $I4/mcm$  phase pointing out the stability of the coherent JT effect in that phase.

The  $\text{Os}_{\parallel}$  and  $\text{Os}_{\perp}$  (figure 6(0.5-d)) are negative and decreases (increases in absolute value) raising the pressure toward the orthorhombic to tetragonal transition. Differently from  $x=0$  and  $x=0.25$  samples  $\text{Os}_{\parallel}$  and  $\text{Os}_{\perp}$  present very similar values as a function of pressure in the orthorhombic phase. The  $Pnma$  to  $I4/mcm$  phase transition provokes the drop of  $\text{Os}_{\parallel}$  and the change of sign of  $\text{Os}_{\perp}$  which absolute values increases steeply from  $\sim 1\%$  to about 3-4 %.

#### D. $\text{La}_{0.33}\text{Ca}_{0.67}\text{MnO}_3$

The structural evolution of  $\text{La}_{0.33}\text{Ca}_{0.67}\text{MnO}_3$  as a function of the applied pressure (figure 6(0.67-a,b)) closely resemble that of  $\text{La}_{0.5}\text{Ca}_{0.5}\text{MnO}_3$  with a first order  $Pnma$  to  $I4/mcm$  phase transition. However, this transition occurs at a lower pressure, that is around 13 GPa, for  $x=0.67$  sample. The two phases coexist till about 19 GPa. As for the  $x=0.5$  sample, we do not have evidences of a pre-transition effect below the orthorhombic to tetragonal phase transition. Fitting of the  $V(P)$  curve with a third order Birch-Murnaghan equation<sup>35</sup> gives the bulk modulus  $B_0=210$  GPa and its pressure derivative at zero pressure  $B'=2$  (table III) in the  $Pnma$  phase. In the  $I4/mcm$  phase, the bulk modulus slightly decreases to  $B_0 \approx 190$  GPa. The refinement of the atomic positions point to three different Mn-O distances

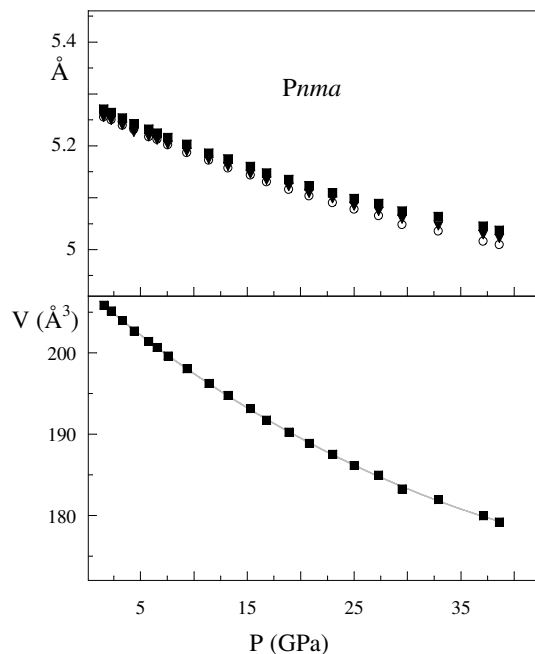


FIG. 7: Lattice parameters (upper panel) and volume (lower panel) for  $\text{CaMnO}_3$  sample. The continuous grey line represent the fitting of  $V(P)$  with a B-M equation of state.

in the  $Pnma$  phase (figure 6(0.67-c)), distinguishable over the statistical uncertainty raising the pressure above  $\approx 3$  GPa. The maximum differences between the three Mn-O distances is achieved at around 8-10 GPa where the JT distortion reach about 0.08 Å. At higher pressures, the differences become progressively smaller. In the region of coexistence of orthorhombic and tetragonal phases it is difficult to achieve a good refinement of atomic positions, however two distinct Mn-O distances are observed in the high pressure tetragonal phase suggesting the stability of the coherent JT effect in that high pressure phase.

As for the other samples the  $\text{Os}_{\parallel}$  and  $\text{Os}_{\perp}$  (figure 6(0.67-d)) are negative and decreases (increases in absolute value) raising the pressure toward the orthorhombic to tetragonal transition. We notice that  $\text{Os}_{\parallel}$  and  $\text{Os}_{\perp}$  are similar in the  $Pnma$  phase, and have similar trend, as already found in  $x=0.5$  sample and differently from  $x=0$  and  $x=0.25$  samples. The orthorhombic to tetragonal phase transition is characterized by a large discontinuity in  $\text{Os}_{\perp}$  increasing from  $\sim -1\%$  to more than 4%.

#### E. $\text{CaMnO}_3$

In  $\text{CaMnO}_3$ , unlike all the other compounds along in this series, no phase transition was detected up to 45 GPa (figure 7). As described before, there are only  $\text{Mn}^{4+}$  manganese ions in this compound, which adopt a low spin configuration and no Jahn-Teller distortion. The stability of the  $\text{CaMnO}_3$  structure under applied pressure

TABLE V: Refined structural parameters from refinement of  $\text{La}_{0.33}\text{Ca}_{0.67}\text{MnO}_3$  XRD patterns at selected pressures in the  $Pnma$  and  $I_4/mcm$  space groups. Numbers in parentheses are statistical errors at the last significant digit. The atomic positions in the  $Pnma$  are: Mn (0., 0., 0.5); La and O(1): ( $x$ , 0.25,  $z$ ); O(2) ( $x, y, z$ ). In the  $I_4/mcm$  space group the atomic positions are: Mn (0., 0., 0.); La/Ca and O(1) (0., 0., 0.25) and O(2) ( $x$ ,  $x+0.5$ , 0.).

	3.5 GPa ( $Pnma$ )	19.1 GPa ( $I_4/mcm$ )
$a(\text{\AA})$	5.3386(4)	5.1444(4)
$b(\text{\AA})$	7.5273(5)	7.6152(7)
$c(\text{\AA})$	5.3698(4)	
$V(\text{\AA}^3)$	215.79(1)	201.53
La/Ca $x$	0.089(6)	
$z$	0.0145(6)	
O(1) $x$	0.576(6)	
$z$	0.002(2)	
O(2) $x$	0.275(5)	0.286(1)
$y$	0.0217(1)	
$z$	0.693(3)	
$R_{WP}$ %	2.40	2.23
$\chi^2$	0.3	0.9

demonstrates that  $\text{Mn}^{3+}$  doping is essential in stabilizing the high pressure tetragonal phase.

The  $V(P)$  curve in  $\text{CaMnO}_3$  sample has been fitted with a third order Birch-Murnaghan equation giving  $B_0=171$  GPa and  $B'=5.9$ . In this sample,  $B_0$  slightly decreases with respect to the value found in  $x=0.67$ . This decreasing trend contrasts the increasing of  $B_0$  as a function of  $x$  found in the other samples. This effect is partially due to the neglect of fourth order terms in the B-M fitting that, in addition, gives a quite large  $B'$  that contrasts with the isotropic compressibility of this structure. The fourth order fit (table III) gives indeed a larger  $B_0 \sim 195$  GPa and a lower  $B' \sim 2.9$ .

#### IV. DISCUSSION

The plots in figure 6 describe the structural phase diagram of  $\text{La}_{1-x}\text{Ca}_x\text{MnO}_3$  as a function of composition and applied pressure. The extreme compounds remain orthorhombic in the whole pressure range investigated. Nevertheless the  $\text{LaMnO}_3$  depicts a complex evolution of the cell edges and a  $Pnma$  to  $Imma$  phase transition that are absent in the  $\text{CaMnO}_3$  sample, where the only effect of pressure is the isotropic squeezing of the unit cell. This difference must be related to the JT nature of  $\text{Mn}^{3+}$  ions, in  $x=0$  samples, opposite to the undistorted  $\text{MnO}_6$  octahedra in  $x=1$  samples.

All the doped compounds, at low pressure, are in the orthorhombic phase and evolve toward a tetragonal one

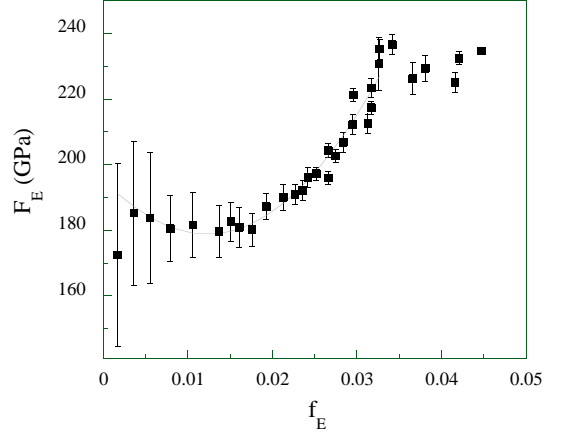


FIG. 8: Normalized pressure  $F_E = P/3f_E(1+2f_E)$  versus the Eulerian strain  $f_E = \frac{(V/V_0)^{2/3} - 1}{2}$  for  $x=0.25$  sample.  $V_0$  is the cell volume at ambient conditions.

on raising the pressure. This phase transition is closely related to the Ca doping: the onset of orthorhombic to tetragonal transition moves to a lower pressure as the Ca content increases. Moreover, the nature of this transition is different in the hole doped ( $x < 0.5$ ) and in the electron doped ( $x \geq 0.5$ ) composition regions: in  $x=0.25$  the transition appears smooth and the presence of intermediate parasitic phases can be hypothesized on the basis of the reduced refinement accuracy (larger  $\chi^2$ ). On the contrary the  $x=0.5$  and  $x=0.67$  samples depict first order  $Pnma$  to  $I_4/mcm$  transition.

The increasing of Ca content has a clear effect on the energetic cost for the orthorhombic to tetragonal transition ( $\Delta E = P\Delta V$ ). For  $x=0.75$  the  $Pnma$ - $I_4/mcm$  phase transition is very smooth and we found  $\Delta V = V(\text{tetra}) - V(\text{ortho}) = -0.53 \text{ \AA}^3$  at  $P = 26.4$  GPa, giving to  $\Delta E = -8.4$  KJ/mole. For  $x=0.50$   $\Delta V = 1.07 \text{ \AA}^3$  at  $P=19.5$  GPa corresponding to  $\Delta E = -12.56$  KJ/mole and, for  $x=0.33$   $\Delta V = 2.33 \text{ \AA}^3$  at  $P=17.33$  GPa, corresponding to a  $\Delta E = -24.33$  KJ/mole. This means that on increasing the Ca doping the tetragonal phase needs more energy to be stable and this is confirmed by the progressive widening of the coexistence region of the two phases in figure 6. To explain this finding, we notice that the  $Pnma$  structure responds to the hydrostatic compression not only by squeezing the  $\text{MnO}_6$  octahedra but also by acting on their relative orientation, i.e. changing the Mn-O-Mn bond angle, that is less expensive for the energetic balance. In the  $Imma$  and  $I_4/mcm$  phases, the tilting mode changes and the octahedra are aligned along one direction: along the  $[101]$  direction in the  $Imma$  phase (figure 3b) and along the  $b$  axis in the  $I_4/mcm$  phase (figure 3c). Moreover, the coordination for the cation (La/Ca) changes from 8 ( $Pnma$ ) to 10-12 in the  $I_4/mcm$ - $Imma$  phase. These changes make the structure more rigid as confirmed by the overall increasing of the lattice stiffness across the  $Pnma$ - $I_4/mcm$  phase transi-

tion (table III).

All the doped compounds, in a range of the high pressure region, exhibit an evident splitting of Mn-O distances signalling the enhancement of coherent JT distortions. The analogous trend has been already reported for  $x=0.25$  sample<sup>27</sup>. Moreover in  $x=0.5$  and  $x=0.67$  samples two Mn-O distances remains well distinct even in the high pressure tetragonal phase. These findings, together with previous high pressure resistivity<sup>27</sup>, Raman<sup>26</sup> and infra red<sup>25</sup> spectroscopy results, demonstrate that, at high pressures, a mechanism competes with the pressure induced reduction of the distortions and charge delocalization, as observed at the low pressures<sup>19,23</sup>. This mechanism is largely unexpected on the basis of a model involving only DE and e-p interactions. In fact squeezing the structure raises  $e_g$  electron hopping integral; thus, increased pressure is expected to enhance the charge mobility. In addition, since the polaron stability is inversely proportional to the charge mobility, the squeezing of the structure is expected to bring the system in a less distorted-metallic phase, in contrast to the experimental result, at least in some regions of the high pressure-concentration phase diagram.

To explain these findings, other mechanisms must be taken into account, and these could be the cooperative

JT effect and the SE coupling. The stability of JT distortion is related to the difference between the energy gained by the on-site distortion and the energy spent by the lattice to bring about such a distortion. In case of cooperative JT effect, the ordered orbital allow for alternating elongated and compressed Mn-O bonds, reducing the net lattice distortion, thus making the JT polaron energetically more stable. This effect has been invoked<sup>22</sup> to explain the pressure induced stabilization of a low temperature CO phase to the detriment of FM phase in  $(\text{Nd,Sm})_{0.5}\text{Sr}_{0.5}\text{MnO}_3$  perovskites. On the other side the SE coupling, being fundamental in stabilizing the CO phases in  $x \geq 0.5$  compounds, must also play a role. Theoretical simulations have indeed suggested the possibility of FM to CO phase transition as a function of the SE coupling strength<sup>39,40</sup>.

We have studied structural the high pressure phase diagram of  $\text{La}_{1-x}\text{Ca}_x\text{MnO}_3$  perovskites. Our findings detail the peculiar structural evolution of sample structure as a function of pressure and composition and suggest that squeezing the structure under hydrostatic pressure has a profound effect on the relative strength of the involved interactions, namely DE, SE and charge to lattice coupling.

---

\* Corresponding author: meneghini@fis.uniroma3.it

† INFM-OGG c/o ESRF Grenoble, France

<sup>1</sup> C. Zener, Phys. Rev. **82**, 403 (1951).

<sup>2</sup> P. Anderson and H. Hasegawa, Phys. Rev. **100**, 675 (1955).

<sup>3</sup> P. de Gennes, Phys. Rev. **118**, 141 (1960).

<sup>4</sup> A. J. Millis, P. B. Littlewood, and B. I. Shraiman, Phys. Rev. Lett. **74**, 5144 (1995).

<sup>5</sup> A. J. Millis, B. I. Shraiman, and R. Mueller, Phys. Rev. Lett. **77**, 175 (1996).

<sup>6</sup> P. Schiffer, A. P. Ramirez, W. Bao, and S.-W. Cheong, Phys. Rev. Lett. **75**, 3336 (1995).

<sup>7</sup> M. Fernández-Díaz and et al., Phys. Rev. B **59**, 1277 (1999).

<sup>8</sup> T. Ohsawa and J. Inoue, Phys. Rev. B **65**, 14401 (2001).

<sup>9</sup> C. H. Booth, F. Bridges, G. H. Kwei, J. M. Lawrence, A. L. Cornelius, and J. J. Neumeier, Phys. Rev. B **57**, 10440 (1998).

<sup>10</sup> P. G. Radaelli, D. E. Cox, M. Marezio, S. W. Cheong, P. E. Schiffer, and A. P. Ramirez, Phys. Rev. Lett. **75**, 4488 (1995).

<sup>11</sup> D. Louca and T. Egami, Phys. Rev. B **59**, 6193 (1999).

<sup>12</sup> D. Louca, T. Egami, W. Dmowski, and J. F. Mitchell, Phys. Rev. B **64**, 180403 (2001).

<sup>13</sup> A. Lanzara, N. L. Saini, M. Brunelli, F. Natali, A. Bianconi, P. G. Radaelli, and S. W. Cheong, Phys. Rev. Lett. **81**, 878 (1998).

<sup>14</sup> C. Meneghini, C. Castellano, S. Mobilio, A. Kumar, S. Ray, and D. D. Sarma, J. Phys. Cond. Mat. **14**, 1967 (2002).

<sup>15</sup> G. Subías, J. García, J. Blasco, M. C. Sánchez, and M. G. Proietti, J. Phys.: Cond. Mat. **14**, 5017 (2002).

<sup>16</sup> F. Bardelli, C. Meneghini, S. Mobilio, C. Castellano, and V. Dediu, Nucl. Inst. and Met. B **200**, 226 (2003).

<sup>17</sup> H. Y. Hwang, S.-W. Cheong, P. G. Radaelli, M. Marezio, and B. Batlogg, Phys. Rev. Lett. **75**, 914 (1995).

<sup>18</sup> H. Yoshizawa, R. Kajimoto, H. Kawano, Y. Tomioka, and Y. Tokura, Phys. Rev. B **55**, 2729 (1997).

<sup>19</sup> H. Y. Hwang, T. T. M. Palstra, S. W. Cheong, and B. Batlogg, Phys. Rev. B **52**, 15046 (1995).

<sup>20</sup> A. Nossrov, J. Pierre, J. Beille, V. Vassiliev, and B. Slobodin, Eur. Phys. J. B **6**, 467 (1998).

<sup>21</sup> J. J. Neumeier, M. F. Hundley, J. D. Thompson, and R. H. Heffner, Phys. Rev. B **52**, 7006 (1995).

<sup>22</sup> Y. Tokura, H. Kuwahara, Y. Moritomo, Y. Tomioka, and A. Asamitsu, Phys. Rev. Lett. **76**, 3184 (1996).

<sup>23</sup> V. Laukhin, J. Fontcuberta, J. L. Garcia-Munoz, and X. Obradors, Phys. Rev. B **56**, 10009 (1997).

<sup>24</sup> R. Senis, V. Laukhin, B. Martinez, J. Fontcuberta, X. Obradors, A. A. Arsenov, and Y. M. Mukovskii, Phys. Rev. B **57**, 14680 (1998).

<sup>25</sup> A. Congeduti, P. Postorino, P. Dore, A. Nucara, S. Lupi, S. Mercione, P. Calvani, A. Kumar, and D. D. Sarma, Phys. Rev. B **63**, 184410 (2001).

<sup>26</sup> A. Congeduti, P. Postorino, E. Caramagno, M. Nardone, A. Kumar, and D. D. Sarma, Phys. Rev. Lett. **86**, 1251 (2001).

<sup>27</sup> C. Meneghini, D. Levy, S. Mobilio, M. Ortolani, M. Nunez-Reguero, A. Kumar, and D. D. Sarma, Phys. Rev. B **65**, 12111 (2001).

<sup>28</sup> C. Schulze, U. Lienert, M. Hanfland, M. Lorenzen, and F. Zontone, J. Synchrotron Rad. **5**, 77 (1998).

<sup>29</sup> H. K. Mao, J. Xu, and P. M. Bell, J. Geophys. Res. **91**, 16491 (1986).

<sup>30</sup> A. P. Hammersley, S. O. Svensson, M. Hanfland, A. N. Fitch, and D. Hauserman, High Pressure Res. **14**, 235 (1998).

- (1996).
- <sup>31</sup> A. C. Larsson and R. B. von Dreele, Report LAUR **86-748**, Los Alamos National Laboratory, Los Alamos, New Mexico (1999).
  - <sup>32</sup> F. Birch, Phys. Rev. **71**, 809 (1947).
  - <sup>33</sup> I. Loa, P. Adler, A. Grzechnik, K. Syassen, U. Schwarz, M. Hanfland, G. K. Rozenberg, P. Gorodetsky, and M. P. Pasternak, Phys. Rev. Lett. **87**, 125501 (2001).
  - <sup>34</sup> P. G. Radaelli, M. Marezio, H. Y. Hwang, and S.-W. Cheong, J. Solid State Chem. **122**, 444 (1996).
  - <sup>35</sup> F. J. Birch, J. Geophys. Res. **91**, 4949 (1986).
  - <sup>36</sup> L. Pinsard-Gaudart, J. Rodriguez-Carvajal, A. Daoud-Aladine, I. Goncharenko, M. Medarde, R. I. Smith, and A. Revcolevschi, Phys. Rev. B **64**, 64426 (2001).
  - <sup>37</sup> P. M. Woodward, T. Vogt, D. E. Cox, A. Arulraj, C. N. R. Rao, P. Karen, and A. K. Cheetham, Chem. Mater. **10**, 3652 (1998).
  - <sup>38</sup> A. M. Glazer, Acta Cryst. **B28**, 3384 (1972).
  - <sup>39</sup> S. Yunoki, T. Hotta, and E. Dagotto, Phys. Rev. Lett. **84**, 3714 (2000).
  - <sup>40</sup> S. Fratini, D. Feinberg, and M. Grilli, Europ. Phys. J. p. to be published (2001).